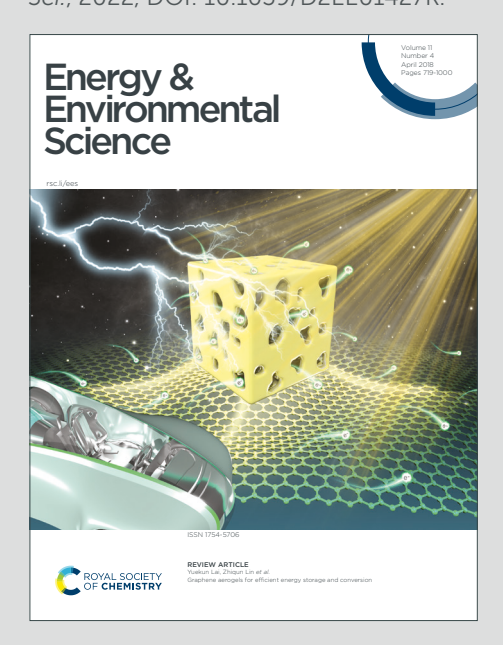


# Energy & Environmental Science



**Accepted Manuscript** 

This article can be cited before page numbers have been issued, to do this please use: H. Liu, N. Agrawal, A. Ganguly, Y. Chen, J. Lee, J. Yu, W. Huang, M. M. Wright, M. Janik and W. Li, *Energy Environ. Sci.*, 2022, DOI: 10.1039/D2EE01427K.



This is an Accepted Manuscript, which has been through the Royal Society of Chemistry peer review process and has been accepted for publication.

Accepted Manuscripts are published online shortly after acceptance, before technical editing, formatting and proof reading. Using this free service, authors can make their results available to the community, in citable form, before we publish the edited article. We will replace this Accepted Manuscript with the edited and formatted Advance Article as soon as it is available.

You can find more information about Accepted Manuscripts in the <u>Information for Authors</u>.

Please note that technical editing may introduce minor changes to the text and/or graphics, which may alter content. The journal's standard <u>Terms & Conditions</u> and the <u>Ethical guidelines</u> still apply. In no event shall the Royal Society of Chemistry be held responsible for any errors or omissions in this Accepted Manuscript or any consequences arising from the use of any information it contains.



## **Broader Context**

It is critical to combat against global warming and stabilize global temperature to the manageable level of +1.5°C by curbing CO<sub>2</sub> emissions, eventually achieving zero net emissions by 2050. This target requires the significant deployment of renewable energy and clean hydrogen in all industry sectors. Particularly, hydrogen produced from water electrolysis provides a promising route to decarbonation of industry and transportation. However, the dominant energy loss in traditional water electrolyzers is the unfavorable thermodynamics and slow kinetics of oxygen evolution reaction at the anode. In this work, an efficient bipolar hydrogen production system was demonstrated by combining cathodic hydrogen evolution from water and anodic hydrogen generation from aldehyde oxidation. Unlike conventional combined systems for hydrogen production that require high voltage (>1.0 V) and are limited by mass transport (<100 mA cm<sup>-2</sup>) of reactants, this study doubled the hydrogen production rate to achieve industrial-level current density with economic viability. Biorenewable furfural (a model aldehyde) with a large production scale suggests another green hydrogen source of biomass. The successful implementation of such an energy-efficient process will seamlessly integrate renewable electricity (from wind, solar) and renewable carbon sources, thus impacting future distributed manufacturing of green hydrogen and carbon chemicals with lowenergy consumption and low-carbon footprint.

View Article Online DOI: 10.1039/D2EE01427K

## **ARTICLE**

# Ultra-Low Voltage Bipolar Hydrogen Production from Biomass-Derived Aldehydes and Water in Membrane-Less Electrolyzers

Hengzhou Liu,<sup>‡a</sup> Naveen Agrawal,<sup>‡b</sup> Arna Ganguly,<sup>‡c</sup> Yifu Chen,<sup>a</sup> Jungkuk Lee,<sup>a</sup> Jiaqi Yu,<sup>d</sup> Wenyu Huang,<sup>d</sup> Mark Mba-Wright,<sup>\*c</sup> Michael J. Janik,<sup>\*b</sup> Wenzhen Li<sup>\*a</sup>

 Received 00th January 20xx,
 Accepted 00th January 20xx

DOI: 10.1039/x0xx00000x

Water electrolysis using renewable energy inputs is being actively pursued as a green route for hydrogen production. However, it is limited by the high energy consumption due to the sluggish anodic oxygen evolution reaction (OER) and safety issues associated with H<sub>2</sub> and O<sub>2</sub> mixing. Here, we replaced OER with an electrocatalytic oxidative dehydrogenation (EOD) of aldehydes for bipolar H<sub>2</sub> production and achieved industrial-level current densities at cell voltages much lower than during water electrolysis. Experimental and computational studies suggest a reasonable barrier for C-H dissociation on Cu surfaces, mainly through a diol intermediate, with a potential-dependent competition with the solution-phase Cannizzaro reaction. The kinetics of EOD reaction was further enhanced by a porous CuAg catalyst prepared from a galvanic replacement method. Through Ag incorporation and its modification of the Cu surface, the geometric current density and electrocatalyst durability were significantly improved. Finally, we engineered a bipolar H<sub>2</sub> production system in membrane-electrode assembly-based flow cells to facilitate mass transport, achieving a maximum current density of 248 and 390 mA cm<sup>-2</sup> at cell voltages of 0.4 V and 0.6 V, respectively. The faradaic efficiency of H<sub>2</sub> from both cathode and anode reactions attained ~100%. Taking advantage of the bipolar H<sub>2</sub> production without the issues associated with H<sub>2</sub>/O<sub>2</sub> mixing, an inexpensive, easy-to-manufacture dialysis porous membrane was demonstrated to substitute the costly anion exchange membrane, achieving an energy-efficient and cost-effective process in a simple reactor for H<sub>2</sub> production. The estimated H<sub>2</sub> price of \$2.51/kg from an initial technoeconomic assessment is competitive with US DoE's "Green H<sub>2</sub>" targets.

## 1. Introduction

Hydrogen can serve as an energy carrier in clean, efficient, sustainable, and cost-attractive energy systems.<sup>1</sup> The full environmental benefit of moving toward a hydrogen society is to realize its production from renewable resources including water or biomass.<sup>2, 3</sup> "Green H<sub>2</sub>" produced from renewable energy sources can then be used in fuel cells to supply electricity for stationary and transportation applications.<sup>1</sup>

Water electrolysis is the most attractive and sustainable approach for future  $H_2$  generations;  $^{1,\ 4}$  however, current water electrolyzers are limited by their high cost, largely due to the thermodynamically and kinetically sluggish oxygen evolution

Rather than producing  $H_2$  from water electrolysis, biomass-derived aldehydes are excellent alternative candidates to water as the energy and H-source for  $H_2$  production.<sup>2</sup> The effectiveness of aldehyde conversion to  $H_2$  depends on the discovery of catalytic/electrocatalytic processes, and catalytic materials to enable such processes. Catalytic  $H_2$  generation from biobased aldehydes can also be accompanied by the production of valuable by-products, such as carboxylic acids. In the past years, the transformation of aldehydes to carboxylic acids along with  $H_2$  evolution was reported from several non-Faradaic reactions, including base-,  $^{17, 18}$  heterogeneous-,  $^{19-21}$ 

reaction (OER).5, 6 In addition, the gas crossover, between unbalanced gas pressures of cathodic H2 (two-electron transfer) and anodic O<sub>2</sub> (four-electron transfer), can induce explosive H<sub>2</sub>/O<sub>2</sub> mixtures, and the produced reactive oxygen species could damage the membranes, leading to safety concerns.7, 8 Expensive ionexchange membranes are commonly used to separate gaseous products,9 and developing suitable low-cost, easy-to-manufacture membrane materials is still in need.<sup>9, 10</sup> One strategy to address the above-mentioned problems is to replace OER with anodic reactions that are thermodynamically more favorable and economically more attractive, with the potential to produce valuable products rather than O2.11 Despite significant progress on developing paired electrolyzers for H<sub>2</sub> production, an electrolytic voltage of >1.0 V on non-noble metal catalysts is still required. 12-16 Moreover, limited by mass transport of reactants in the aqueous phase, the current density is usually <100 mA cm<sup>-2</sup>,<sup>11</sup>, <sup>15</sup> severely restricting their industrial-relevant applications.

a. Department of Chemical and Biological Engineering, Iowa State University, 618 Bissell Road, Ames, IA 50011, USA. E-mail: wzli@iastate.edu, mjj13@psu.edu, markmw@iastate.edu.

b. Department of Chemical Engineering, Pennsylvania State University, State College, PA 16801, USA.

<sup>&</sup>lt;sup>c</sup> Department of Mechanical Engineering, Iowa State University, Ames, IA 50011, USA.

<sup>&</sup>lt;sup>d</sup> Department of Chemistry, Iowa State University, 618 Bissell Road, Ames, IA 50011, USA.

e. †Electronic Supplementary Information (ESI) available: [details of any supplementary information available should be included here]. See DOI: 10.1039/x0xx00000x

f. ‡ These authors contributed equally to this work.

This article is licensed under a Creative Commons Attribution-NonCommercial 3.0 Unported Licence

Article. Published on 12 August 2022. Downloaded on 8/16/2022 1:55:52 PM

**Journal Name** 

```
Electrochemical, Faradaic half-reactions:
EOD: 2R-CHO + 4OH^- = 2R-COO^- + 2H_2O + 2e^- + H_2 (RXN 1)
ECO: R-CHO + 3OH^- = R-COO^- + 2H_2O + 2e^- (RXN 2)
Thermocatalytic, non-Faradaic overall reactions:
R-CHO + OH = R-COO + H-H(H<sub>2</sub>)
                                              (RXN 3)
Cu^{2+} + 2RCHO + 4OH^{-} = Cu + 2RCOO^{-} + 2H_2O + H_2 (RXN 4)
Disproportionation reaction (Cannizzaro reaction):
2R-CHO + OH = R-COO + R-CH<sub>2</sub>OH
. . . . . . . . . . . . . . . . . . .
```

Scheme 1. Comparison of reactions of aldehydes.

and homogeneous<sup>22-25</sup>-catalyzed processes (RXN 3). However, these reactions generally require a high concentration of base (>>1 M OH-) or elevated temperature (>100 °C) with both aldehyde and  $H_2O$  as proton sources in the formation of H2. The condition of high alkalinity/temperature is prone to favor aldehyde degradation toward humin-based polymers, largely suppressing the selectivity towards desirable acid and H<sub>2</sub>. <sup>25, 26</sup> Another aldehyde-based chemical process, namely, electroless deposition (ELD) of metals (e.g., Cu, RXN 4) onto conductive or nonconductive substrates, has been applied to recycle metals or develop flexible printed circuits. 27-29 This non-Faradaic process occurs by reducing metal salts in solutions where the electrons are supplied from the reducing agents, e.g., formaldehyde (HCHO), and H2 is co-produced through aldehyde oxidation catalyzed by in-situ reduced metallic Cu.30 More important, due to the non-Faradaic nature of above reactions, they are unsuitable to replace anodic OER for bipolar H2 generation in the electrolytic cell.

Alternatively, Wang et al. recently reported an electrocatalytic oxidative dehydrogenation (EOD) pathway on Cu electrode, in which the aldehyde oxidation cogenerated H<sub>2</sub> and carboxylic acid (RXN 1) at anodic potentials near 0 V (vs. RHE).  $^{\rm 31,\ 32}$  The EOD process is fundamentally distinct from conventional electrochemical oxidation (ECO, RXN 2) of aldehydes, which requires higher anodic potentials and forms acid and protons. 15, 33-37 The facile kinetics of the EOD reaction enable pairing with the hydrogen evolution reaction (HER) at low cell voltages, evolving gaseous H<sub>2</sub> from both electrodes while producing carboxylic acids in the anode effluent. Despite the successful demonstrations of EOD on Cu, detailed mechanistic questions remain. Why is Cu unique for EOD, compared to high overpotentials for furfural ECO on Pt and Au? In strong alkaline solutions, the non-Faradaic Cannizzaro transformation from aldehydes (RXN 5) is a major side reaction that cannot be ignored.<sup>38</sup> The competition between this non-Faradaic path and the EOD reaction is not well explored, leaving open questions that must be answered to enable effective reaction engineering for this process.

In this work, we elucidated the mechanism for the EOD reaction, and combined it with the cathodic HER for bipolar "green H2" production at cell voltages well below those needed for water electrolysis. Biomass-derived furfural was selected as the model aldehyde for EOD reaction because the conversion of inedible lignocellulose to furfural is well established, currently conducted industrially on a scale of 0.43 million tons/year.<sup>39-41</sup> The oxidative carboxylic acid product [e.g., 2-furoic acid (2-FA)] is a crucial precursor for renewable polymer polyethylene furanoate (PEF) in drinking bottle manufacturing.<sup>42</sup>

Our experimental and computational results reveal a common gem-diol intermediate with a reasonable Charrier39602EEatalyst mediated C-H dissociation to make 2-FA and H<sub>2</sub> on the Cu surface, competing with the solution phase Cannizzaro reaction and showing potential-dependent kinetics. Through combined electrokinetic observations and DFT calculations, we demonstrate that Cu optimally balances the ability to activate the gem-diol C-H bond, form the C-O(H) bond, avoid CO poisoning, and be stable in metallic form at the desired operating potentials. Since the EOD reaction on a Cu electrode is driven by anodic potentials with onsets as low as ~0.1 V<sub>RHE</sub>, we further used a galvanic replacement method to etch Cu foam to create a CuAg catalyst with higher roughness for facile EOD kinetics. Protected by Ag layers, the stability of this Cu-based catalyst is significantly improved under electrolysis conditions of high alkalinity and anodic biasing. Moreover, we developed a membraneelectrode assembly (MEA)-based electrolysis system for bipolar H<sub>2</sub> production with faradaic efficiencies (FEs) from both cathode and anode near ~100%. Taking advantage of the facile kinetics on CuAg catalysts and increased mass transport resulting from the porous substrate and rough catalyst layer, we demonstrated a maximum current density of  $\rm H_2$   $(j_{A-H_2})$  of 248 mA cm $^{-2}$  at a cell voltage of 0.4 V. Considering that H<sub>2</sub> was co-produced from cathode and anode without H<sub>2</sub>/O<sub>2</sub> mixing issues, an inexpensive, easy-to-manufacture dialysis filter membrane as a porous separator was employed to separate organic reactants and replace the costly anion exchange membrane (AEM). Techno-economic analysis (TEA) of a commercial process based on the bipolar H<sub>2</sub> production exhibited potential economic viability with co-generation of value-added carboxylic acids.

## 2. Results and Discussion

## 2.1 Evaluating transition-metal catalysts for the EOD reaction

The EOD of furfural was first studied in an H-type reactor with various commercially available metallic foams or foils as catalysts (Fig. S1-2, ESI†). Linear sweep voltammetry (LSV) was conducted with and without furfural in 1 M KOH. As shown in Fig. 1a, LSV curves on Cu foam with 200 mM furfural showed an apparent current density in the potential range of 0.1-0.5 V<sub>RHE</sub>, corresponding to the EOD reaction. Half-hour chronoamperometry (CA, Fig. 1b) tests at 0.2 and 0.4 V<sub>RHE</sub> (V<sub>RHE</sub>: potential versus reversible hydrogen electrode) showed that the production rate ratio of 2-FA to H<sub>2</sub> is close to 2:1, in line with the stoichiometry of the EOD equation (RXN 1). The FEs of 2-FA and H<sub>2</sub>, defined as the moles of 2-FA or 2 times of moles of H<sub>2</sub> produced at the Cu electrode divided by the total moles of electrons applied, are both ~100%.

The EOD current density increases initially as the potential is shifted anodically until the onset of Cu oxidation. The optimum potential range of 0.1-0.4 V<sub>RHE</sub> for EOD is below the thermodynamic potential of Cu oxidation toward  $Cu_2O$  (0.46  $V_{RHE}$ , pH = 14, **Table S5**, ESI†). Additional control experiment on a Cu<sub>2</sub>O coated catalyst showed a negative current density at 0.4  $V_{\text{RHE}}$ , indicating no Cu oxidation occurs at this potential (Fig. S3, ESI†). The current density was gradually approached zero suggesting the reduction of Cu<sub>2</sub>O to Cu. These observations align with the previous experimental (using in-situ grazing incidence XRD<sup>43, 44</sup>) and computational<sup>45</sup> works that the surface Cu oxide layer is fully reduced to metallic Cu at anodic potentials of 0.3-0.4 V<sub>RHE</sub>. These results all suggested metallic Cu is

Science Accepted Manu

**Journal Name** ARTICLE

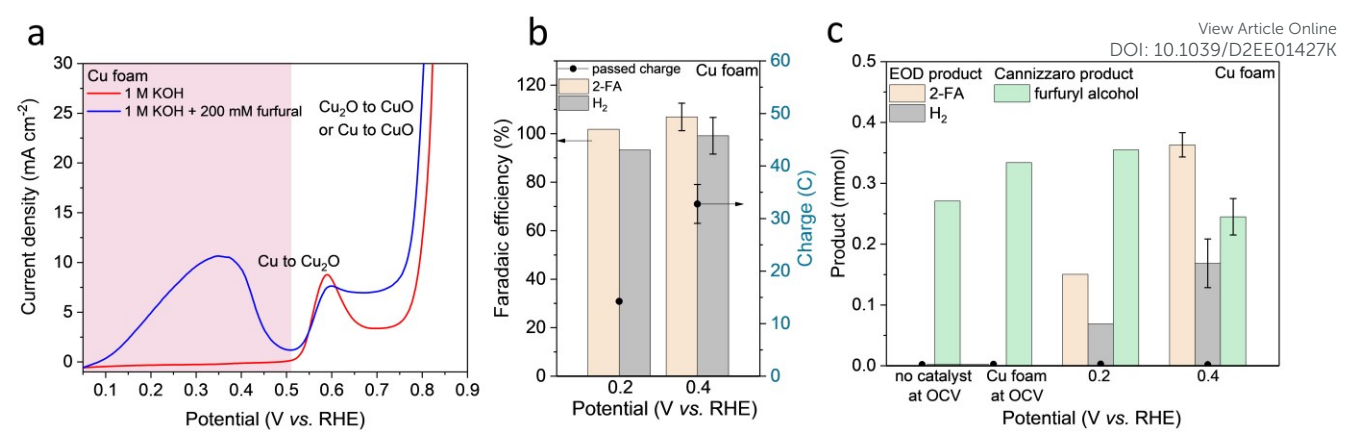
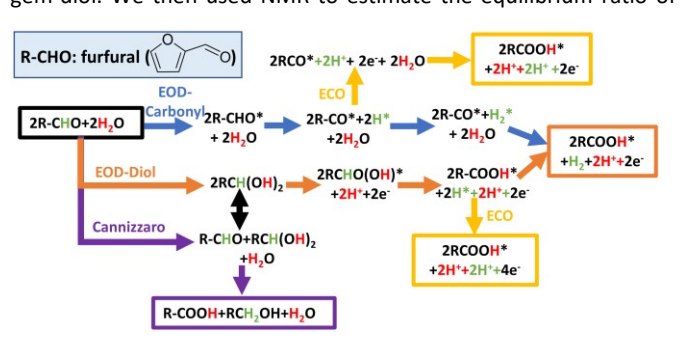


Fig. 1 EOD reaction on Cu foam. (a) LSV (2<sup>nd</sup> cycle) on Cu foam (1 cm<sup>2</sup>) with or without 200 mM furfural in 1 M KOH electrolyte. (b) Faradaic efficiency (left yaxis) and passed charge (right y-axis), and (c) product for half-hour electrolysis in 1 M KOH with 200 mM furfural at open circuit voltage or different applied potentials.

the active phase for EOD catalysis. The detailed physical characterization of our self-prepared Cu-based catalysts for EOD were shown in the section 2.3.

A similar EOD reaction was observed on Ag foil with an onset potential of ~0.3 V<sub>RHE</sub> (Fig. S4, ESI†), positively shifting ~200 mV compared to the Cu foam. Interestingly, the occurrence of the EOD reaction was not observed on other transition metals (Fig. S5, ESI†). For Pd, Pt, Au and Ni electrodes, no apparent current density was observed in the relatively low anodic potential regions, and no detectable H<sub>2</sub> was obtained from our online-gas chromatography (GC). These results suggested Cu and Ag are unique metal catalysts for the EOD reaction, with Cu demonstrating higher current density and lower overpotential.

Furfuryl alcohol detected in the electrolyte is hypothesized to be generated from the competing, non-Faradaic Cannizzaro pathway. The reported FE and production rate of 2-FA from the EOD pathway is calculated after subtracting 2-FA co-produced from the Cannizzaro reaction (quantified from the amount of furfuryl alcohol produced). Fig. 1c shows that the Cannizzaro reaction is the only reaction occurring under open circuit voltage (OCV) without a catalyst. Interestingly, the presence of catalyst (i.e., Cu foam at OCV) promoted this non-Faradaic reaction. The results with Ag foil, and Cu and Ag nanoparticles under OCV also showed the elevated Cannizzaro reaction rates (Table S1, ESI†). When the applied potential increased from 0.2 to 0.4 V<sub>RHE</sub> (Fig. 1c), the EOD pathway became more favorable, suppressing the Cannizzaro reaction. This potential dependent competition suggests these two reactions share a common intermediate, which could be a deprotonated form of gem-diol. We then used NMR to estimate the equilibrium ratio of



Scheme 2. Proposed reaction mechanisms for EOD, ECO, and Cannizzaro reactions.

aldehyde to gem-diols. Fig. S6 shows that 68% of furfural existed as its diol form in the 0.1 M KOH solution, and this value approached ~100% when the base concentration increased to  $\geq$  0.5 M. Thus, the diol species, produced from a chemical (or solution-mediated) step with OH- attacking the aldehyde, is the common intermediate involved in both the EOD and Cannizzaro reactions. The EOD reaction could involve the adsorption of this diol species on the electrode surface followed by the C-H bond cleavage to produce H<sub>2</sub>.

## 2.2 DFT calculations

The proposed reaction mechanisms for aldehyde EOD, ECO, and Cannizzaro reactions are shown in Scheme 2. Per molecule of furfural consumed, the ECO, EOD, and Cannizaro are 2,1, and 0 electron transfer reactions. The equilibrium conversion between the shared gem-diol intermediate (R-CH(OH)<sub>2</sub>) for the Cannizaro or EOD (diol route) and the reactant aldehyde is noted with a black arrow signifying the connection between these paths. In the alkaline medium, this gem-diol intermediate might preferentially deprotonate to the gem-diol anion.

Our electrochemical results in section 2.1 above show that the oxidation of furfural to furoic acid can occur on Cu at significantly lower potentials (0.1 V<sub>RHE</sub>) than Au or Pt (0.9 V<sub>RHE</sub>); and revealed an alternative low overpotential reaction (EOD) with H<sub>2</sub> co-generation or alcohol co-generation through the Cannizzaro reaction. We rationalize the experimental findings through DFT calculated intermediate species binding energies and elementary reaction energetics.

Earlier studies on furfural electro-oxidation (ECO) on transition metal surfaces suggest that the binding of CO\* is a key activity descriptor for catalytic activity. 46 At low potentials, a high coverage of strongly bound CO\* could be formed through the thermal decarbonylation of furfural. This has been long recognized for formaldehyde electro-oxidation on Pt electrodes. 47 Due to strong CO\* binding (-1.63 eV), Pt requires an anode potential of ~0.9 V<sub>RHE</sub> to observe noticeable furfural oxidation current. Binding of CO\* on Cu (-0.63 eV) is substantially weaker than on Pt, allowing Cu to avoid the CO\* poisoning issues observed on Pt catalysts (Table S2, ESI†). Au surfaces also bind CO\* weakly (0.15 eV), though large overpotentials are still observed experimentally due to inherently low activity for C-H bond dissociations (as discussed below).

Our prior DFT results, in collaboration with experimental efforts of Holewinski and co-workers, concluded that ECO of furfural can

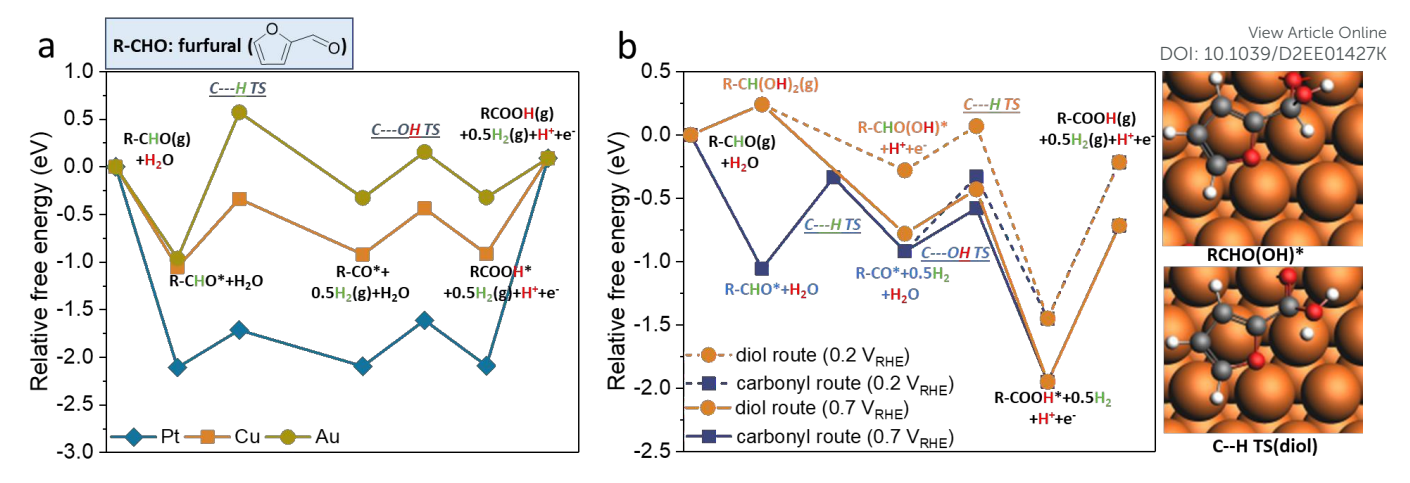


Fig. 2 Reaction free energy diagrams for EOD paths on late transition metal (111) surfaces. (a) Comparison of relative free energy on Pt/Cu/Au (111) surfaces for EOD of furfural using the carbonyl route. (b) Potential dependent relative free energies for carbonyl and diol routes on the Cu(111) surface. Inset figures show the adsorbed RCHO(OH)\* optimized structure and C-H dissociation transition state in the diol mechanism, both on the Cu(111) surface.

proceed through either a carbonyl or a solution-assisted diol route on transition metal catalysts. <sup>48</sup> On Au catalysts, the diol route is preferred due to weaker binding of the furanic ring, and requires a significant oxidative overpotential due to the poor activity of Au for the C-H dissociation step inside the diol route. <sup>48</sup> Cu better balances weak CO\* binding and C-H activation, as well as H\* and OH\* binding, to enable the low potential EOD process (albeit, requiring alkaline conditions for stability, whereas Au and Pt can be used in acid as well).

The key distinction between the EOD and ECO through the perspective of elementary steps is only the step involving the surface bound H\* derived from C-H cleavage (Scheme 2), which either converts to a proton through a reverse-Volmer step (yellow arrow) or a half mole of hydrogen through a Tafel step (orange and bule arrows). The preference between the EOD and ECO mechanism is indirectly dictated by a combination of thermodynamic (CO\*, H\*, OH\*, and FCHO/FCOOH\* binding energies) and kinetic descriptors (C-H and C-OH activation). Table S2 shows the comparison of key thermodynamic descriptors. Fig. 2a shows the reaction free energy diagram for the EOD reaction at  $0.2\ V_{RHE}$  through the carbonyl route on Pt(111), Cu(111), and Au(111) surfaces. The desorption energy of 2-FA(FCOOH) is likely overestimated on all metals due to solvation effects, as discussed in our prior work.<sup>48</sup> Ignoring the desorption of furoic acid, C-H cleavage for the EOD mechanism is the limiting step on all three metals. Among the three metals, Pt has the lowest C-H barrier (0.39 eV) for the EOD mechanism. However, EOD has not been observed on Pt despite it being a great HER catalyst. This is because Pt requires significant overpotential (0.9  $V_{\text{RHE}}$ ) to become electrocatalytically active for furfural oxidation due to CO\* poisoning. At such high potentials, the reverse Volmer step is highly favorable, and the ECO process occurs instead of EOD. Contrarily, Au binds H\* quite weakly (+0.38 eV) but is limited by slow C-H activation (1.54 eV barrier) still requiring significant oxidative overpotentials beyond the EOD feasibility region where H\* stays bound to surface. Cu has a moderate barrier for C-H cleavage (0.72 eV) and intermediate H binding (+0.31 eV), suggesting that at low potentials, a Tafel step might be preferrable over the reverse-Volmer step, leading to the EOD mechanism.

The H\* in an EOD/ECO reaction is produced from the non-electrochemical C-H cleavage of either the adsorbed aldehyde (R-CHO\*) in the "carbonyl route" or the hydrolyzed form of the

aldehyde (R-CH(OH)<sub>2</sub>) in the "diol route". The preference between the carbonyl and diol route for EOD is dependent on the concentration ratio of diol to furfural in the solution and the applied potential. Experiments in this study show that the concentration of diol increases as the concentration of base increases. Fig. 2b compares the reaction free energy diagram for the carbonyl (blue) and diol route (orange) on Cu (111) at 0.2 and 0.7 V<sub>RHE</sub>. At 0.2 V<sub>RHE</sub>, there is no clear preference between the two routes, but as the potential is made more positive (0.7 V<sub>RHE</sub>), the adsorption (with an electron transfer) of the deprotonated diol (R-CHO(OH)) becomes more favorable by 0.5 eV. Determining the exact potential at which the diol route dominates is challenging, as it requires comparing adsorption and surface reaction energies, and determining adsorption thermodynamics in the solvated system is challenging. However, the diol route appears viable on Cu electrodes, with its dominance increasing over the carbonyl route as potential increases.

The experimentally observed suppression of the Cannizzaro reaction relative to the EOD reaction at higher potentials can be explained by the potential dependent free energy diagram of EOD vs. the non-Faradaic Cannizzaro reaction in Fig. S7, ESI†. The common intermediate between the two pathways is the diol (RCH(OH)<sub>2</sub>) or its deprotonated form in a basic medium (RCHO(OH-)). The energetics in Fig. S7 show formation of the adsorbed deprotonated ion becomes more favorable at more positive potentials due to the involvement of electron transfer during adsorption. More favorable adsorption promotes the rate of surface mediated C-H cleavage, and therefore the EOD reaction becomes more competitive with the Cannizaro reaction as potential is increased. The precise potential at which EOD becomes competitive with the solution phase Cannizaro reaction is challenging to determine with DFT, due to the imprecision in evaluation of solution phase energetics and approximations of using a single crystal Cu surface and a single surface coverage.

It is challenging for DFT methods to examine the relative rates of H\* oxidation (reverse Volmer step) and  $H_2$  evolution, which will depend on the relative activation barriers for these two steps, as well as the surface coverage of H\* and effective concentration of OH-near the surface. Rapid C-H dissociation from the aldehyde/diol would allow establishing a high coverage of H\* species, and higher coverage would promote  $H_2$  evolution relative to H\* oxidation.

IVIronmental Science Accepted Manuscri

**ARTICLE Journal Name** 

## 2.3 Unifying EOD reaction with CuO<sub>x</sub> reduction by aldehydes within a chemical looping scheme

In addition to the occurrence of EOD reaction on metallic Cu electrode (Faradaic half-reaction), we examined the chemical reaction of copper oxide with furfural, as half of an overall chemical looping reaction in which copper is oxidized, then reduced by furfural while producing furoic acid and hydrogen products. As we discuss here, the copper oxide reduction step is analogous to the EOD reaction, in that the chemical reaction can be considered as a coupling of a copper oxide reduction half-reaction, with the copper metal produced by this reaction then catalyzing the EOD reaction as the oxidation half-reaction.

When an oxidized Cu foam was immersed in the electrolyte, H<sub>2</sub> spontaneously evolved. The H<sub>2</sub> production rate increased then decreased with progressing time (Fig. S9, ESI†). Further experiments were performed in a batch reactor with 1 M KOH + 200 mM furfural, and 50 mg Cu<sub>2</sub>O or CuO nanoparticles (NPs) under Ar atmosphere (Fig. S10a-b, ESI+). H<sub>2</sub> production shows a similar volcano-type production rate with time, as initial copper oxide reduction produces Cu metal that accelerates the EOD reaction, until consumption of copper oxide slows the reduction half-reaction. No H<sub>2</sub> was detected in the control experiments with Cu NPs, as H<sub>2</sub> is only detected when the Cu NPs was intentionally oxidized prior to reaction with the aldehyde. XRD confirmed that oxidized Cu was reduced back to its metallic state after the reaction (Fig. S10c, ESI+), indicating Cu oxides were indeed consumed during H<sub>2</sub> evolution. In addition, the ratio of production rate of 2-FA and H<sub>2</sub> on all oxidized Cu is close to 2:1, consistent with the stoichiometry of the EOD reaction. Furthermore, when fully deuterated (D2O with 1 M NaOD) solution was used, differential electrochemical mass spectroscopy (DEMS) showed only m/z signal of 2, confirming both H atoms in H<sub>2</sub> are from the aldehyde group (Fig. S10d, ESI†), which is in line with the EOD reaction. The chemical reduction of CuO<sub>x</sub> nanoparticles effectively behaves as a "short-circuited" combination of CuO<sub>x</sub> reduction (equilibrium potential of CuOx reduction is 0.3-0.4 V<sub>SHE</sub>, Table S4-5, ESI†) and the EOD reaction (Fig. 3c), with the effective mixed potential presumably varying between the two potentials based on the relative rates of the two half-reactions as the reaction progresses to equilibrium.<sup>49, 50</sup>

In addition, as shown in Fig. S11 and Table S4-5, reduction of Ag<sub>2</sub>O with aldehydes also leads to H<sub>2</sub> production, whereas reduction of Pt(II) and Pd(II) does not evolve H<sub>2</sub>.51 This is in agreement with the electrochemical furfural oxidation studies discussed above, in which furfural ECO will occur rather than EOD once Pt and Pd metal are formed.

Overall, we reported EOD and Cu/CuOx chemical looping reactions showing H<sub>2</sub> generation (Fig. S12c, ESI†) that is distinct to the previously reported ECO of aldehyde toward acid without H<sub>2</sub> production on high oxidation states of Cu (Fig. S12a, ESI†)<sup>33, 52</sup> or through Cu(I)/Cu(II) redox cycling (Fig. S12b, ESI†)16, 53. The major reason is that Cu (0) is active for the EOD reaction, but Cu(I)/Cu(II) is not. The EOD reaction is shown to occur as the oxidation half reaction during simultaneous chemical reduction of CuO<sub>x</sub> by aldehydes. The metallic Cu is required for EOD due to both higher activity for C-H dissociation and the Tafel H-H formation step.

## 2.4 Demonstrating an active and stable CuAg catalyst for **EOD** reaction

To further improve EOD kinetics on metallic Cu, we prepared an oxide-derived Cu (OD-Cu) electrode via an electrooxidation-thermal treatment method (details in Methods). In addition to its high surface area, oxide-derived catalysts are highly active view for rtic yarjous electrochemical reactions because of their unique fleatures such as low coordinated sites, grain boundaries, and subsurface oxygen. 54-57 However, under steady-state electrolysis (EOD reaction) at 0.2 V<sub>RHE</sub>, a fast decay was observed during five continuous half-hour electrolysis periods (Fig. 3h), resulting in a 71% drop of H<sub>2</sub> production rate, along with a loss of the Cu nano-sized morphology and surface roughness (Fig. S13, ESI+).

Inspired by the approaches of using a noble metal (e.g., Pd, Rh) to induce surface reconstruction and stabilize Cu substrates, 58-60 we prepared bimetallic CuAg catalysts (through galvanic replacement and electrodeposition methods). We chose Ag as the second metal to add to Cu because Ag is expected to be more durable<sup>61</sup> and Ag was also observed to catalyze the EOD reaction. A Cu-rich, nano-sized CuAg catalyst prepared from the galvanic replacement method (denoted as CuAggiv/Cu) facilitates the EOD reaction with higher intrinsic activity and stability. The as-synthesized CuAgglv/Cu catalyst was prepared by immersing pre-cleaned Cu foam in AgNO<sub>3</sub> solution under sonication to create an oxidized porous Cu surface with large area (Fig. 3a) and well-dispersed Ag on and underneath the Cu-rich surface (as shown in EDS, Fig. S14, ESI†). Roughening of the surface is a result of rapid Cu crystal deformation that started from the grain boundaries and defects.<sup>62</sup> XRD analysis indicated that both metals are polycrystalline with Cu<sub>2</sub>O, Cu, and Ag phases (Fig. 3b). Auger electron spectra of Cu LM (Fig. 3c) with a kinetic energy peak at ~916.8 eV suggested the surface is dominated by Cu<sub>2</sub>O species, while Ag 2p spectra showed its metallic state (Fig. S15, ESI†). HRTEM and EDS mapping also suggested the uniform distribution of Ag on Cu and a clear phase separation between Ag and Cu<sub>2</sub>O (Fig. S16, ESI†).

Extensive measurements were conducted on CuAgglv/Cu anode in the three-electrode H-type cell to test its performance for the EOD reaction. The as-synthesized CuAg $_{\rm glv}$ /Cu was first held in-situ at -0.1V<sub>RHE</sub> for 3 min to reduce surface Cu<sub>2</sub>O back to metallic Cu in the furfural-containing electrolyte. XRD and Auger Cu LM spectra showed a significant decrease in Cu<sub>2</sub>O intensity after this treatment (Fig. S17, ESI†). We further compared the intrinsic activity of various Cu-based electrodes [CuAgglv/Cu, OD-Cu, and commercial Cu NPs coated on Cu foam (Cu NPs/Cu)], normalizing their activity by quantitatively determining their surface areas. Double-layer capacitance was measured to assess the roughness of each material and then normalized to the plain Cu foam (Fig. S18, ESI†). LSV curves with roughness factor (RF)-normalized current density showed a similar trend among those Cu-based catalysts (Fig. 3d). Typically, CuAgglv/Cu exhibited four times higher intrinsic activity (in the RFnormalized current density) than Cu NPs/Cu at 0.4 V<sub>RHE</sub>. In addition, we observed a slightly higher RF-normalized current density of the oxide-derived CuAggIv/Cu than the OD-Cu (20.2 vs. 17.7 mA cm<sup>-2</sup> at 0.4 V<sub>RHE</sub>), suggesting an active oxide-derived Cu-rich surface was obtained by a simple galvanic replacement method, which effectively improved EOD reaction performance.

EOD activity on CuAggiv/Cu was further tested at static electrolysis conditions at different potentials. Online DEMS with a pulsed potential of 0.4 V<sub>RHE</sub> confirmed the proton source for H<sub>2</sub> in the EOD reaction is the aldehyde group rather than H<sub>2</sub>O (**Fig. 3f-g**). With the constant electrolysis duration (half-hour), Fig. 3e shows ~100% FE of both 2-FA and H<sub>2</sub> (production rate ratio of ~2:1, Fig. S19, ESI†) in the potential range of 0.1-0.5 V<sub>RHE</sub>. The passed charge (Fig. 3e, right y-axis) increased from 0.1 to 0.4 V<sub>RHE</sub> followed by a decrease starting from 0.5 V<sub>RHE</sub>. Specifically, the maximum current density of  $H_2$  at the early stage of electrolysis at 0.4  $V_{RHE}$  attained ~250 mA cm<sup>-2</sup>

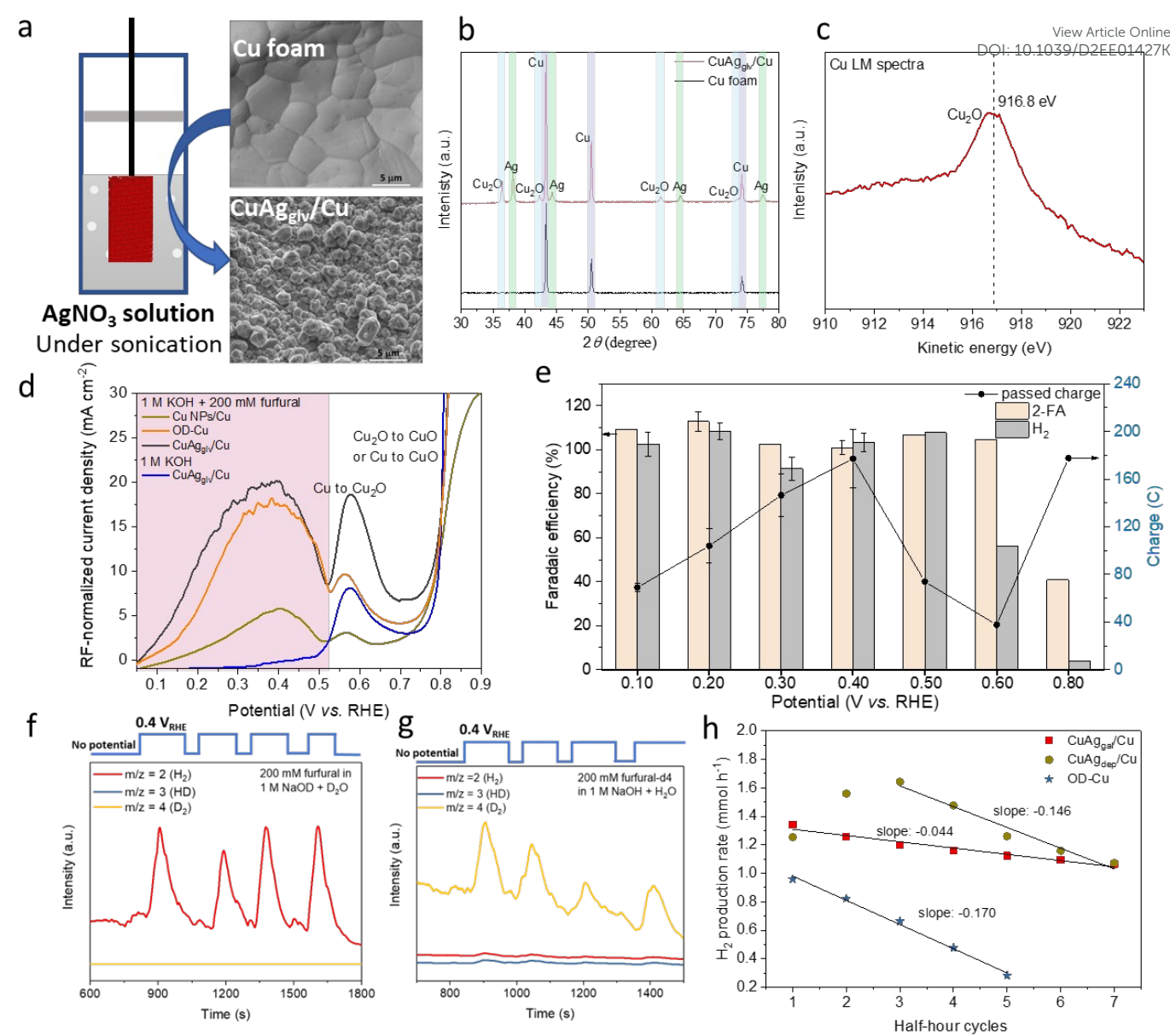


Fig. 3 EOD reaction on CuAg<sub>glv</sub>/Cu in H-type cell. (a) Scheme of galvanic replacement method and SEM images of Cu foam and as-synthesized CuAg<sub>glv</sub>/Cu. (b) XRD patterns of Cu foam and as-synthesized CuAg<sub>glv</sub>/Cu. (c) Auger Cu LM spectrum of as-synthesized CuAg<sub>glv</sub>/Cu. (d) Linear sweep voltammetry ( $2^{nd}$  cycle) on Cu-based electrodes, including Cu NPs/Cu, OD-Cu, CuAg<sub>glv</sub>/Cu, with or without 200 mM furfural in 1 M KOH electrolyte. The current density was normalized to the roughness factor (RF). (e) Faradaic efficiency (left y-axis) and passed charge (right y-axis) in 1 M KOH with 200 mM furfural at different applied potentials on CuAg<sub>glv</sub>/Cu for half-hour electrolysis. The geometric area for the electrode was 1 cm². (f)-(g) DEMS signals at m/z = 2, 3, and 4 at a pulsed potential of 0.4  $V_{RHE}$  on CuAg<sub>glv</sub>/Cu electrode. Measurements in two deuterated electrolytes were performed: (f) 200 mM furfural in D<sub>2</sub>O with 1 M NaOD and (g) furfural-d4 in H<sub>2</sub>O with 1 M NaOH. (h) H<sub>2</sub> production rate at different numbers of cycle for independent half-hour electrolysis with different Cu-based electrodes: OD-Cu, CuAg<sub>glv</sub>/Cu, and CuAg<sub>dep</sub>/Cu. Fresh electrolyte was replaced after each half-hour electrolysis. The slopes show their degradation rate.

(Fig. S19, ESI†), and the gradual decease in current density was attributed to the consumption of furfural during electrolysis. The EOD performance can be further increased by conducting electrolysis in flow cells (details shown in Section 2.4). The decrease in reaction activity at higher potentials is due to the gradual oxidation of Cu to Cu(I), which is unable to catalyze the EOD reaction. The decrease in FE ratio of  $H_2$  and 2-FA from ~1 to 0.5 at 0.6  $V_{RHE}$  suggests the concurrent occurrence of EOD (RXN 1) and ECO (RXN 2) reactions. Additional support for Cu(I) not being active was demonstrated by the relatively low EOD activity on a drop-coated  $Cu_2O/Cu$  catalyst (Fig. S20, ESI†). Further increase in the anodic potential to 0.8  $V_{RHE}$  largely

increased the passing charge to a relatively high value (178 C), but with significantly suppressed H $_2$  formation (FE: ~4%). This could be due to the further oxidation of Cu and Cu (I) to Cu(II) that switched the dominant pathway from the EOD to the ECO reaction.  $^{16}$ ,  $^{33}$ ,  $^{53}$ ,  $^{63}$  The favorable ECO reaction on copper oxides could be due to their weak binding of surface H or low H coverage due to slow C-H activation, suggesting the dominant pathway between EOD and ECO reactions can be well-regulated by anodic potentials and/or chemical states of Cu.

The catalyst synthesis conditions of sonication and precursor concentrations are critical to obtaining fully etched and oxidized Cu surface, which strongly affects EOD activity. The concentration of

**Environmental Science Accepted Manuscri** 

AgNO $_3$  offers a tunable driving force to manage the surface roughness and relative abundance of Cu $_2$ O in the as-synthesized CuAg $_{glv}$ /Cu (Fig. S21, ESI $^{\dagger}$ ). Changing its concentration from 1 to 200 mM is equivalent to a  $^{\sim}0.14$  V Nernstian shift of the redox potential (Supplementary Methods, ESI $^{\dagger}$ ). We observed that a higher concentration of AgNO $_3$  is needed to form a Cu $_2$ O-dominated precatalyst; however, using too concentrated AgNO $_3$  (>100 mM) excessively dissolved the Cu surface and decreased the surface

roughness (Fig. S21, ESI†), leading to a drop of EOD activity.

Journal Name

To further study the function of Ag and how its distribution on the Cu foam substrate affecting the EOD durability, CuAg<sub>glv</sub>/Cu was compared with a CuAg catalyst obtained from the electrodeposition method (i.e., CuAg<sub>dep</sub>/Cu). Different from the porous surface of CuAg<sub>glv</sub>/Cu created from the driving force beween two metals with spontaneous deposition of Ag and exchange with Cu, the mesoporous architectures of CuAg<sub>dep</sub>/Cu were generated by H<sub>2</sub> bubbles from the concurrent HER under strong acid conditions (1.5 M H<sub>2</sub>SO<sub>4</sub>).<sup>58</sup> The use of sufficiently large cathodic current density (2 A cm<sup>-2</sup>) minimized the spontaneous galvanic replacement, and the diffusion of metal ions dominantly governed their deposition onto the electrode. Therefore, a linear relationship between the atomic percentage of incorporated Ag in the electrode (as determined by ICP) and the molar percentage of precursor Ag+ in the deposition solution was established (Fig. S22-23, ESI†). From this plot, the Ag loading at 12.5 at% for  $CuAg_{dep}/Cu$  (same as  $CuAg_{glv}/Cu$ ) can be wellcontrolled by tuning Ag+ percentage in the deposition solution.

SEM showed the dendritic Ag and hexagonal Cu morphologies on the CuAg<sub>dep</sub>/Cu surface with microporous high-surface-area, exhibiting a higher RF than CuAg $_{glv}$ /Cu (14.2 vs. 4.5, **Fig. S22-23, ESI†**). However, the durability for EOD reaction showed a different trend between these two catalysts (Fig. 3h). At 0.2 V<sub>RHE</sub>, CuAg<sub>dep</sub>/Cu showed an increased H<sub>2</sub> production rate in the first three half-hour cycles and outperformed CuAg<sub>glv</sub>/Cu electrode, mainly benefiting from the higher surface area of CuAg<sub>dep</sub>/Cu. Nevertheless, CuAg<sub>dep</sub>/Cu activity degraded faster than CuAg<sub>glv</sub>/Cu as shown by different slopes for degradation rate: -0.146 vs. -0.044. Crosssectional SEM and EDS images (Fig. S24-26, ESI+) pre- and postelectrolysis exhibited different Ag distributions between the two electrodes. We observed that the galvanic deposited Ag layer covered the outer shell of the Cu boundary for the CuAgglv/Cu catalyst (Fig. S24-25, ESI+), and this cross-sectional Ag layer still existed after 7-cycle of electrolysis. Resulting from more stable Ag than Cu (as shown in Pourbaix diagrams in Fig. S28, ESI+), the Ag layers in the cross-section partially protected Cu and avoided its quick deactivation under harsh electrolytic conditions. This unique structure could keep a rough and active surface to maintain stability throughout electrolysis. In contrast, cross-sectional SEM-EDS of CuAg<sub>dep</sub>/Cu showed the randomly distributed Ag that loosely covered the Cu substrate (Fig. S26, ESI†), without forming an intact Ag layer at the outer shell of Cu surface. Furthermore, the porous structure of CuAg<sub>dep</sub>/Cu was very fluffy and easy to peel off, leading to physical detachment of Cu and Ag and loss of partial Cu foam substrate after long-term electrolysis (Fig. S26, ESI†). This distinct distribution of Ag and different dynamic surface reconstructions resulted in more durable CuAg<sub>glv</sub>/Cu than CuAg<sub>dep</sub>/Cu. More detailed characterizations and comparisons of the dynamic changes of catalysts are shown in the supplementary information note 2-3, ESI†.

The Ag-decorated Cu electrode showed similar LSV and CA behaviors as the Cu foam substrate and other Cu-based monometallic electrodes, indicating the incorporated Ag did not

directly participate in the EOD reaction to alter product, selectivity, but acted as a promoter to improve intrinsic 1EOD activity and mitigate Cu degradation. In particular, CuAgglv/Cu was able to maintain a higher RF than monometallic Cu. After 5 continuous half-hour electrolysis, the surface of OD-Cu loss its RF (from 3.5 to 1.1) and showing minimal EOD activity, while CuAgglv/Cu showed only slightly decreased activity (21%) and RF (4.5 vs. 4.1, Fig. S33, ESI†) after 7 successive cycles. The assessment clearly demonstrated that Cu-Ag bimetallic catalysts have a faster EOD rate than pure Cu and Ag, indicating that incorporating Ag into Cu engenders a synergistic effect that improves the activity and durability beyond either of its component metals.

With the presence of highly concentrated OH<sup>-</sup> ions in the electrolyte, and more severely, under anodic biasing, the dynamic surface reconstructions occurred during long-term electrolysis. SEM-EDS, XRD, and XPS analysis showed an overall decrease trend in the Cu-to-Ag ratio followed by its increase to the original values. These surface reconstructions were not owing to the detachment of Cu or Ag from the electrode surface to the electrolyte (as confirmed by ICP that Ag atomic percentage was maintained at ~13 at%, **Table S8**, **ESI**†). The mobility of Ag and Cu is significant even at room temperature, and the applied anodic bias during EOD reaction is sufficient to drive drastic changes in their morphology. <sup>64,65</sup> Although the observation of dynamic surface reconstructions, the maintained high surface roughness of CuAg<sub>glv</sub>/Cu during this process still beneficial for robust EOD durability. After sufficient long-term

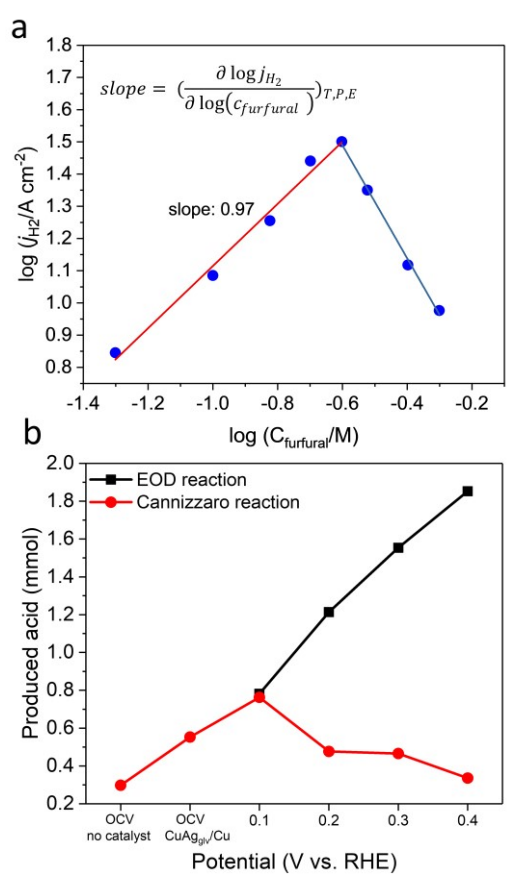


Fig. 4 Electrokinetics of EOD on  $\text{CuAg}_{\text{glv}}/\text{Cu}$  in H-type cell. (a) Dependence of partial current density of  $\text{H}_2$  on furfural concentration. (b) Produced acid from EOD and Cannizzaro reactions at OCV and different anodic potentials in half-hour reaction.

This article is licensed under a Creative Commons Attribution-NonCommercial 3.0 Unported Licence

Open Access Article. Published on 12 August 2022. Downloaded on 8/16/2022 1:55:52 PM

ARTICLE Journal Name

electrolysis, ex-situ SEM-EDS and XPS confirmed the partially detachment of cross-sectional Ag layer and increase in surface oxygen content [towards Cu(OH)<sub>2</sub> and CuO], which could rationalize the experimentally observed 21% drop of the reaction activity after 7 cycles of electrolysis on CuAg<sub>glv</sub>/Cu. Designing Cu-based electrocatalysts with much longer-term durability, especially under harsh electrolytic conditions (e.g., high alkalinity, anodic biasing),  $^{66}$  remains a challenge that needs to be addressed in future studies.

# 2.5 Revealing electrokinetics of EOD reaction on $\text{CuAg}_{\text{glv}}/\text{Cu}$ electrode

To obtain mechanistic insights into the electro-kinetics of EOD, we varied the furfural concentration and plotted the  $j_{A-H_2}$  against its concentration on a log-log scale. The electrolysis was conducted at 0.4  $V_{\rm RHE}$  with the same amount of applied charge of 30 C. We observed a first-order dependence (slope of 0.97) of the furfural-to-H<sub>2</sub> reaction in the furfural concentration range of 50 to 250 mM, and a negative reaction order at concentrations higher than 250 mM (**Fig. 4a**). This negative order can be attributed to the non-Faradaic Cannizzaro reaction (with a reaction order of 2.2 with respect to furfural, **Fig. S34a, ESI†**) that largely outperformed the EOD reaction. As the aldehyde concentration increased, the kinetics for the Cannizzaro pathway increased more rapidly than the EOD route. The Cannizzaro reaction can be largely suppressed by positively shifting the potential from 0.2 to 0.4  $V_{\rm RHE}$  (**Fig. 4b**), in line with our

experimentally and computationally observed potential dependent pathway-switching behavior for the dio Doroute 0.3 Mid half hour electrolysis at 0.4 V<sub>RHE</sub>, the produced 2-FA via the Cannizzaro reaction and EOD reaction were 0.34 and 1.85 mmol, respectively (**Fig. 4b**).

The EOD reaction rate was also highly dependent on the OH-concentration (**Fig. S34b, ESI†**):  $j_{A-H_2}$  linearly increased in the range of 0.1–1 M and reached a plateau at >1.0 M, in line with the NMR results in the formation of gem-diols (**Fig. S6, ESI†**). This highly OH-concentration-dependent rate agreed with our DFT calculated prediction of the more favorable diol route than the direct carbonyl route for the EOD reaction. In addition, half-hour electrolysis of D-labeled furfural (furfural-d4) showed a kinetic isotopic effect (KIE) of 2.06 (calculated from the partial current density ratio of 2-FA, j<sub>H</sub>/j<sub>D</sub>, **Fig. S34c, ESI†**). This large primary KIE suggested the involvement of C-H/D bond cleavage in the rate-determining step (RDS).<sup>67</sup> Electrolysis of furfuryl alcohol on CuAg<sub>glv</sub>/Cu at 0.4 V<sub>RHE</sub> (**Fig. S35, ESI†**) showed minimal current density and undetectable H<sub>2</sub>, indicating that the unique EOD reaction only occurred on the aldehyde group.

The versatility of EOD reaction was also demonstrated by extending the substrate to acetaldehyde (CH $_3$ CHO) and formaldehyde (HCHO), two representative aldehydes with and without  $\alpha$ -H, respectively. It is known that the Cannizzaro reaction occurs only on the compounds without any  $\alpha$ -H, because the formation of critical diol intermediate cannot occur with  $\alpha$ -H

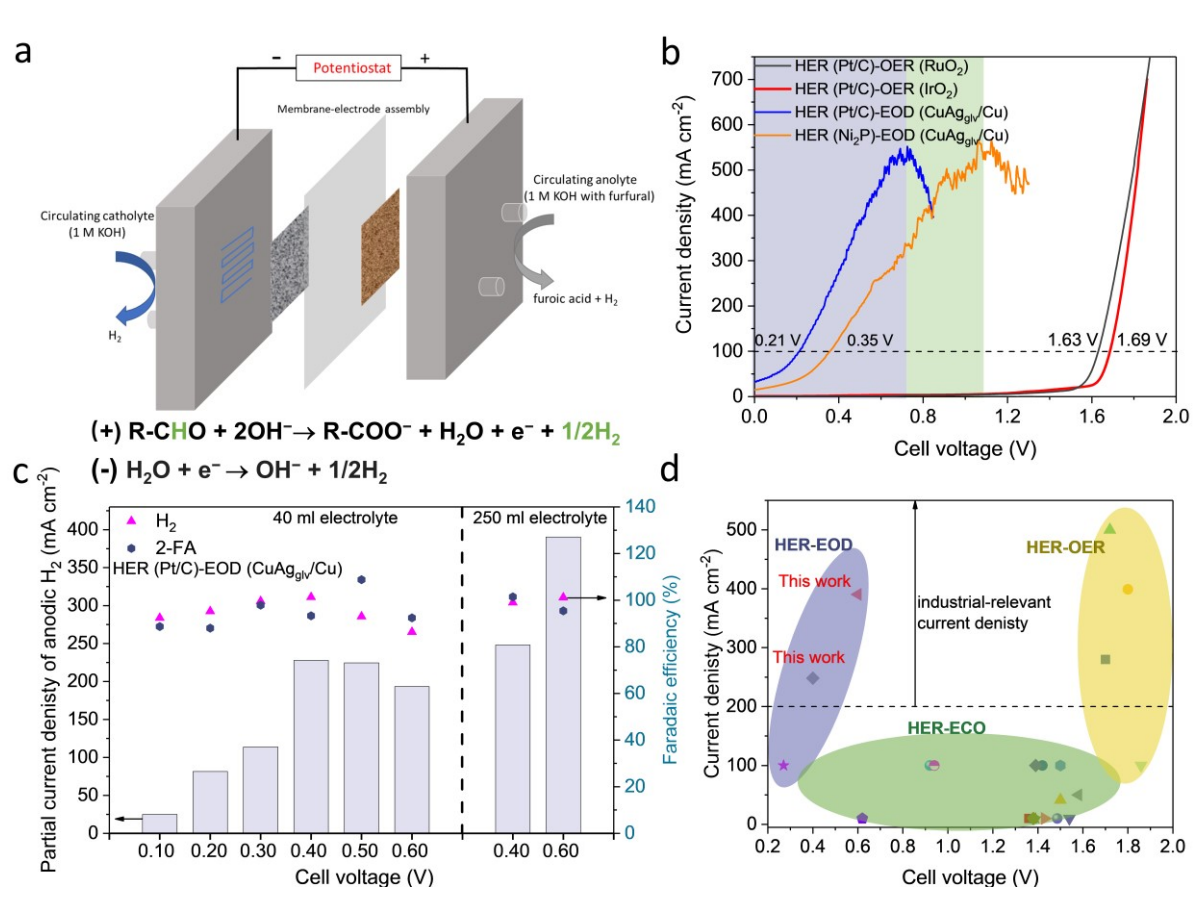


Fig. 5 Bipolar  $H_2$  production in the MEA-based flow cells. (a) Scheme of the flow cell set-up and the reaction equations of bipolar  $H_2$  production. The geometric area of anode was 1 cm<sup>2</sup>. (b) Linear sweep voltammograms for different paired reactions on different electrodes. (c) Partial current denisity of  $H_2$  at different cell voltages with 40 ml and 250 ml electrolyte. HER and EOD reaction were conducted on Pt/C and CuAg<sub>glv</sub>/Cu, respectively. (d) Comparision of the performance of bipolar  $H_2$  production in this work with previous works for electrochemical  $H_2$  production, including HER-ECO paired  $H_2$  production, and HER-OER paired water electrolysis.

rgy & Environmental Science Accepted Manuscri

present.³<sup>8</sup>, <sup>68</sup> The occurrence of EOD reaction, however, did not strongly rely on the type of aldehyde (**Fig. S36, ESI†**), possibly suggesting a direct carbonyl route for EOD reaction. The lower current density for CH³CHO (with  $\alpha\text{-H}$ ) than the reactants without  $\alpha\text{-H}$  indicated that the diol route is more favorable than the direct carbonyl route. These experimental results are all consistent well with DFT calculations. Such versatility can benefit future H² production from EOD of aldehyde feedstocks from different resources.

# 2.6 Developing innovative flow cells for bipolar $\ensuremath{\text{H}_2}$ production

# 2.6.1 $H_2$ production from EOD reaction with enhanced mass transport

Based on the facile EOD kinetics and optimized catalyst morphology and electrolysis conditions, we designed an MEA-based flow cell for bipolar  $H_2$  production (**Fig. 5a**). The MEA consisted of an AEM, a Pt/C cathode, and a CuAg<sub>glv</sub>/Cu anode in a zero-gap configuration. 1 M KOH with and without 250 mM furfural were used as the anolyte and catholyte, respectively.

LSV measurements (**Fig. 5b**) showed that the cell voltage for HER-EOD reaction (0.21 V) was significantly lower than that of HER-OER reaction (1.63 V with RuO<sub>2</sub> anode and 1.69 V with IrO<sub>2</sub> anode) at 100 mA cm<sup>-2</sup>. The current density for HER-EOD reaction increased to the maximum of ~500 mA cm<sup>-2</sup> at 0.7 V, followed by a decrease from >0.7 V, which can be attributed to the oxidation of Cu that switched the reaction pathway toward ECO reaction, in line with H-cell results.

Steady-state, half-hour electrolysis was conducted at different cell voltages (Fig. 5c). The obtained  $j_{A-H_2}$  increased when moving the cell voltage from 0.1 to 0.5 V, and then decreased from >0.6 V. Current density-time profiles (Fig. S37a, ESI†) showed a gradual decrease in the net current density, which is mainly attributed to the consumption of furfural, as the electrokinetic studies have confirmed the 1st order dependence of reaction rate on furfural concentration. To overcome the reactant starvation for half-hour electrolysis, we increased the analyte volume from 40 to 250 mL (Fig. 5c and Fig. **S37b, ESI†**), leading to improvement in  $j_{A-H_2}$  at 248 (0.4 V) and 390 mA cm<sup>-2</sup> (0.6 V). The cell voltages of the HER-EOD system have outperformed most previously reported, conventional electrolyzers for H<sub>2</sub> production, including HER-OER based water electrolyzers and HER-ECO based organic systems (Fig. 5d and Table S9, ESI†). Besides, the bipolar H<sub>2</sub> production system has double the H<sub>2</sub> production rate as compared to the conventional processes where H2 is solely evolved on cathode.

Limited by mass transport, most previously reported partial current densities for organic electrolysis (e.g., furfural, glycerol) to target products are low (i.e. <100 mA cm<sup>-2</sup>) and cannot meet the requirement of industrial applications. 11, 36, 69 Conventional ECO reactions generally need surface reaction of adsorbed reactive oxygen or hydroxyl intermediates and organic-derived intermediates on two adjacent sites via Langmuir-Hinshelwood mechanism, causing severe internal mass-transport issues and limiting the partial current density to desired products. In addition, most ECO reactions [e.g., ECO of furfural or 5-(hydroxymethyl)furfural] are particularly favorable on OER electrocatalysts (e.g., Ni- or Co-based catalysts); therefore, it is challenging to completely suppress OER, especially at high current densities. 11, 69 Thanks to the much favorable thermodynamics (Supplementary note 1, ESI†), the EOD reaction at high current densities occurs at a low potential range of 0.1-0.5 V<sub>RHE</sub>, much lower than the thermodynamic potential of 1.23 V<sub>RHE</sub> for OER, circumventing the Langmuir–Hinshelwood mechanistic sequences that involve adsorbed oxygen species formed at higher potentials 21h addition, the EOD reaction occurs through sequential chemical-electrochemical steps, and the organic species itself is the reactant whose oxidation kinetics is facilitated by single-electron transfer at electrode-electrolyte interface without involving other complicated adsorbates. Besides, the hydrophilic porous Cu foam can facilitate efficient transport of liquid-phase species to the electrode surface, <sup>36,70</sup> and the high porosity and high surface roughness promoted the removal of H<sub>2</sub> bubbles from the surface, so that they do not block the surface for subsequent adsorption of reactants. Overall, benefiting from the favorable thermodynamics, facile kinetics, and largely facilitated external and internal mass transport, we have significantly increased the partial current density of the EOD reaction toward H<sub>2</sub> production.

### 2.6.2 Non-noble metal-based electrocatalyst for HER

Selecting a cathode material with much lower costs than platinum-group metals is crucial for reaching an efficient and costeffective process. To this end, we have prepared a non-precious Ni<sub>2</sub>P catalyst (see Methods, ESI†) with a highly roughened surface. LSV curves in a one-compartment, three-electrode cell showed ~200 mV higher overpotential of Ni<sub>2</sub>P than Pt/C at 100 mA cm<sup>-2</sup>, -0.245 V vs. -0.043 V<sub>RHE</sub> (Fig. S38-39, ESI†), approaching the state-of-art Ni-based catalysts prepared from various methods. 71 We then employed Ni<sub>2</sub>P in the HER-EOD coupled flow system. LSV and CA measurements showed a slightly higher cell voltage (~200 mV shift) than the system with Pt/C cathode (Fig. S40, ESI+). In addition to its lower cost, another advantage of Ni<sub>2</sub>P is that it can suppress electrocatalytic hydrogenation reaction (ECH, Fig. S41, ESI+) in the presence of aldehyde (due to the crossover from anolyte to catholyte as studied in the following section). We tested ECH of furfural at  $-0.15~V_{RHE}$  for a half hour. The result showed a much lower FE toward furfuryl alcohol on Ni<sub>2</sub>P than on Pt/C: 7% vs. 83%. Consequently, if aldehyde crossover occurs during long-term electrolysis, the unfavorable ECH on Ni<sub>2</sub>P would not apparently influence the H<sub>2</sub> evolution from the cathode.

#### 2.6.3 Dialysis membrane as a cost-effective separator

The generation of  $H_2$  from both anode and cathode in the bipolar  $H_2$  production cell can be achieved with a cheap, commercially available filter membrane, namely dialysis membrane. We selected a cellulose-based dialysis membrane with a small pore size [i.e., molecular weight cut-off (MWCO) of 0.1–0.5 kD], which is appropriate for furfural (0.096 kg mol<sup>-1</sup>  $\approx$  0.1 kD) and is stable in acid, base, and organic solutions. Ye

The dialysis membrane was installed in an MEA-based flow cell with Pt/C cathode and CuAggIv/Cu anode (Fig. 6a). The pore size allowed for the free transport of K<sup>+</sup> and OH<sup>-</sup> across the membrane, while furfural crossover from anolyte to catholyte was inhibited. Prior to electrolysis, pretreatment of the membrane in 1 M KOH is necessary for the saturation of membrane pores with ions, reducing the solution resistance across the membrane from 15.37  $\Omega$  to 0.59  $\Omega$  (Fig. S42, ESI†). Based on the high mobility of K<sup>+</sup> and OH<sup>-</sup> without any permselectivity, we calculated theoretical ionic conductivity for dialysis membrane ( $\kappa$  = 247 mS cm<sup>-1</sup>), which is much higher than a typical AEM ( $\kappa$  = 15–20 mS cm<sup>-1</sup>).<sup>73</sup> A slightly higher resistance of the system with dialysis membrane (0.59  $\Omega$ ) than AEM (0.3-0.4 $\Omega$ ) could be due to their different thickness: 70 vs. 28  $\mu$ m. Finally, through operating this dialysis membrane in flow cells, we obtained the

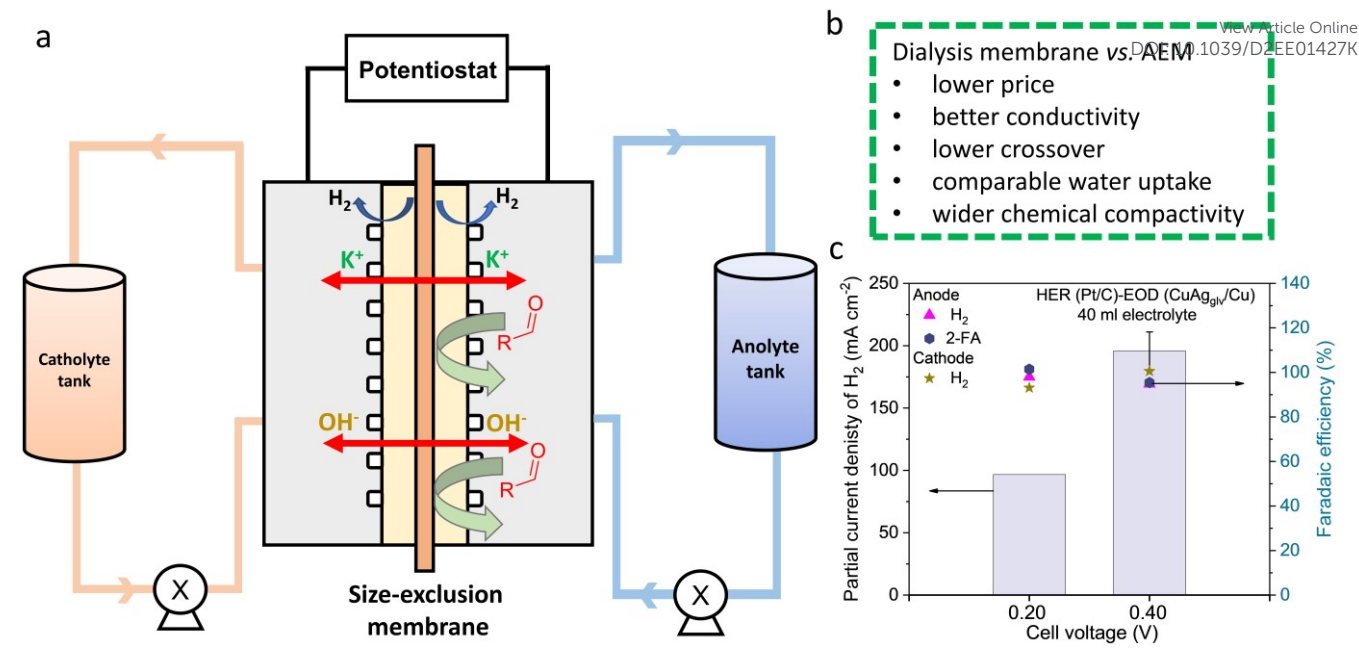


Fig. 6 Bipolar H<sub>2</sub> production in the system with dialysis membrane. (a) Scheme of the flow cell with a dialysis membrane. (b) Comparison between dialysis membrane and AEM. (c) Partial current density of H<sub>2</sub> at different cell voltages with 250 ml of electrolyte.

 $j_{A-H_2}$  of 97 and 216 mA cm<sup>-2</sup> at 0.2 and 0.4 V (**Fig. 6c**), respectively, close to the values in the AEM-based system under the same reaction conditions with 250 ml of electrolyte.

Crossover of gas and liquid products/reactants was analyzed and compared between the systems with AEM and dialysis membrane. Benefiting from the similar H<sub>2</sub> pressures on both anode and cathode during their concurrent generation, ~95% FE of H2 from both electrodes were detected with minimal gas crossover. For half-hour electrolysis at 0.4 V with the dialysis membrane, the liquid products crossover was quantified from the catholyte (Table S10, ESI+), showing 0.34, 2.02, and 4.19 mM of furfural, 2-FA, and furfuryl alcohol, respectively. In comparison, these values for the AEM-based system are 0, 7.15, and 3.67 mM. The total crossover of liquid reactants and products is <11 mM, corresponding to <4.5% of the initial furfural concentration of 250 mM. While the furfural crossover is insignificant for both systems, the crossover of alcohol (produced from Cannizzaro reaction) and acid (generated from EOD reaction) are non-negligible and higher than furfural. Crossover of negatively charged acid product (i.e., C<sub>5</sub>H<sub>3</sub>O<sub>3</sub>- from EOD reaction) is more considerable through the AEM compared to the dialysis membrane, benefiting from the latter's non-selective characteristics for charged and uncharged species. In fact, the permeability of 2-FA [i.e., 5.56  $\times$ 10<sup>-6</sup> cm<sup>2</sup> s<sup>-1</sup>, Fig. S43, ESI†] is one order of magnitude lower than that of the anion selective-AEM [(i.e.,  $2.80 \times 10^{-5} \text{ cm}^2 \text{ s}^{-1}$ ]. In contrast, highly soluble neutral products (i.e., alcohol) are able to crossover through sorption into and subsequent diffusion through the membrane based on the concentration gradient. The slightly higher crossover of furfural alcohol for the dialysis membrane is likely due to its higher water uptake, 74 which was determined to be 38% for the dialysis membrane and 26% for the AEM. Such crossover could be mitigated by optimizing the properties of the dialysis membrane such as reducing the membrane thickness.

Finally, the long-term stability test in the system with dialysis membrane was performed by conducting 7 successive cycles of 1-hour electrolysis at the cell voltage of 0.4 V (Fig. S45, ESI†). Negligible changes in the current density were observed during the first 1–4

hours, followed by a slight decrease in performance from the  $5^{th}$  cycle, showing the excellent stability of both CuAg<sub>glv</sub>/Cu anode and dialysis membrane.

## 2.7 Techno-economic analysis (TEA)

To test the economic feasibility of the system considering capital and operation costs, we provided TEA analysis to quantify the minimum selling price (MSP) of products (details are shown in **supplementary information**). The economic performance of the system is analyzed by using discounted cash flow rate of return (DCFROR) method developed by the National Renewable Energy Laboratory (NREL).<sup>75</sup> We assumed an electrochemical plant capacity of 1500 kg/day H<sub>2</sub>, based on the hydrogen analysis model developed by the U.S. Department of Energy for producing the same hydrogen quantity via water electrolysis.<sup>76</sup>

We first focused on quantifying the MSP of H<sub>2</sub> (Scenario 1), with 2-FA as a byproduct to be sold to the market as the polyethylene 2,5furandicarboxylate (PEF) precursor, which has been proposed to complement polyethylene terephthalate (PET) as a bio-derived plastic. The separation cost of H2 was only considered (Fig. S46a, ESI†). In the system of AEM with Pt/C cathode and CuAg<sub>glv</sub>/Cu anode at a constant capacitance of H<sub>2</sub>, the normalized installed capital costs are highly dependent on the current density, which drastically decreased by around 94% to only \$2.8k/kg(H2) when the current density was increased from 25 to 400 mA cm<sup>-2</sup> (Fig. S47a, ESI†). The much-decreased capital cost is mainly benefiting from the reduced electrolyzer area and electricity cost. Then, the calculated lowest net MSP of H<sub>2</sub> at 400 mA cm<sup>-2</sup> with 0.6 V cell voltage was \$3.2/kg (Fig. 7a), which lies within the range of DOE's target cost of H<sub>2</sub> from electrolyzers. 76, 77 This value is also lower than one of the industrial reported levelized cost of \$4.2/kg and \$3.7/kg for proton exchange membrane (PEM) and AEM electrolyzer, respectively.78 It was observed that the furfural costs contributed the most to the net MSP, and meanwhile, the earned revenue is benefited from the coproduced 2-FA from the bipolar H<sub>2</sub> production system. Under the case of 400 mA cm<sup>-2</sup> and 0.6 V, sensitivity analysis (Fig. S47b, ESI<sup>†</sup>),

Journal Name ARTICLE

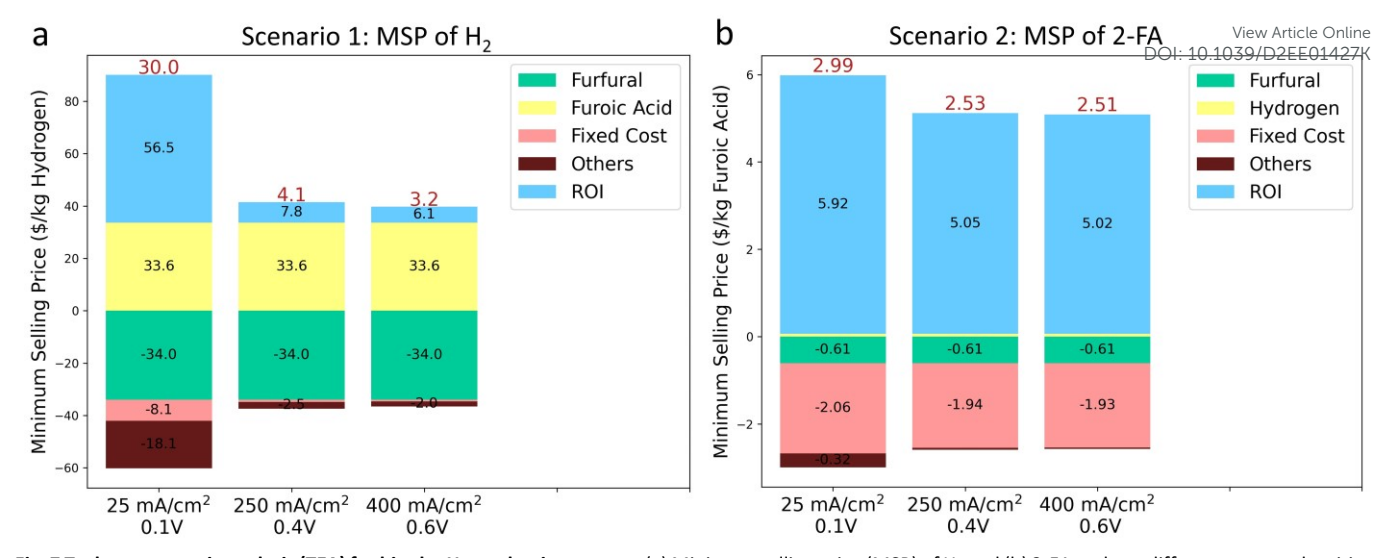


Fig. 7 Techno-economic analysis (TEA) for bipolar H<sub>2</sub> production system. (a) Minimum selling price (MSP) of H<sub>2</sub> and (b) 2-FA at three different current densities and cell voltages. The electrochemical plant capacity is 1500 kg/day of H<sub>2</sub>.

via varying the factors by  $\pm 20\%$ , was performed to determine the key parameters influencing the MSP of  $H_2$ . The market prices of the reactant furfural and the product 2-FA (sold as PET) are two governing factors, and the separation of  $H_2$  showed negligible contribution.

We then quantified the economic viability of the plant by calculating the MSP of 2-FA (**Scenario 2**), with H<sub>2</sub> as the byproduct. In this scenario, the separation cost of both H<sub>2</sub> and 2-FA are considered (**Fig. S46b, ESI†**). The installed capital cost (**Fig. S48a, ESI†**) is the same with Scenario 1, and the different values is owing to the molar mass difference between H<sub>2</sub> and 2-FA. The lowest MSP of 2-FA (i.e., \$2.51/kg) was obtained from the same condition of 400 mA cm<sup>-2</sup> and 0.6 V. Overall, at different voltages and current densities, the estimated MSP ranged between \$2.51 and \$2.99/kg (**Fig. 7b**), comparable to its market price between \$1–\$99/kg (depend on the purity).<sup>79</sup> Different from Scenario 1, the fixed costs and the return on investment (ROI) were the main contributors to expenditure and revenues for MSP of furoic acid. Moreover, the most sensitive parameters that govern the MSP of 2-FA are separation cost and the market price of furfural (**Fig. S48b, ESI†**).

Replacing the cathode catalyst from Pt/C to Ni<sub>2</sub>P has reduced the catalyst cost by 99%. In addition, substitution of AEM by dialysis membrane decreased the electrolyzer cost by 50%. The total installed capital cost and the final MSP in both scenarios did not show significant differences (<5%) by these substitutions, because the major capital cost in an electrochemical plant is the balance of plant (BOP) cost rather than the electrolyzer stacks (Fig. S49-51, ESI†). Nevertheless, the development of cheap, stable, and efficient catalysts and membranes are still the major targets in the research community.

## **Conclusions**

In summary, enabled by the favorable thermodynamics and facile kinetics of EOD reaction, we have achieved bipolar  $\rm H_2$  production in the flow cells with cathodic and anodic FEs of ~100% and current density of 248 and 390 mA cm $^{-2}$  at ultra-low cell voltages of 0.4 V and 0.6 V, respectively. These values are higher than most

previously reported H<sub>2</sub> production rates in the HER-ECO paired systems. Experimental and DFT investigations have elucidated the reaction kinetics of EOD reaction on Cu electrodes, and its linkage to the Cannizzaro reaction. We further explored a more efficient CuAg bimetallic catalyst synthesized on a porous Cu foam electrode, which demonstrated enhanced kinetics, mass transport, and durability. When the flow electrolyzer was engineered with a cost-effective dialysis membrane as a separator, the excellent cell performance and stability were maintained. Moreover, we linked the EOD reaction with a chemical looping reaction and highlighted the possibility of fundamentally bridge electro- and thermo-catalytic reactions, which could help rationally design and predict novel electrocatalysts and processes. The present work provides a novel, robust approach toward sustainable coproduction of hydrogen and carboxylic acids from bio-derived aldehydes. Supported by TEA study, the high efficiency, mild operating conditions, and inexpensive cell components of the approach offer potential for its future development toward a cost-effective process at an industrial scale, holding great promises for revolutionizing the renewable pathways toward clean fuels and biomass-based chemical industry.

#### **Author contributions**

H.L. and W.L. conceived the idea. W.L., M.J., M.M.W. supervised the project. H.L. performed the electrochemical measurements and material synthesis. N.A. and M.J. carried out the DFT calculations. Y.C. revised manuscript and provided constructive suggestions to this work. J.Y. and W.H. performed HRTEM characterization. J.L. performed XRD measurements. A.G. and M.M.W. conduced TEA analysis. All authors discussed the results and contributed to the manuscript writing.

## **Conflicts of interest**

The authors declare no conflict of interest.

## Acknowledgments

This work was supported by the National Science Foundation under grant No. CBET-1947435. W. Li is grateful to his Herbert L. Stiles Faculty Fellowship, the IEC competitive fund (20-IEC-019) and USDA (2021-67021-34650). We thank Drs. Dapeng Jing, Warren E. Straszheim, Carolina Salvati, and Patrick A. Johnston for their assistance with XPS, SEM-EDS, XRD, and ICP-OES measurements. N. Agrawal and M. Janik acknowledge funding from NSF-CBET 1939464 and computational resources provided by Extreme Science and Engineering Discovery Environment (XSEDE), which is supported by National Science Foundation grant number ACI-1053575. N. Agrawal acknowledges training provided by the Computational Materials Education and Training (CoMET) NSF Research Traineeship (DGE-1449785).

#### References

This article is licensed under a Creative Commons Attribution-NonCommercial

Article. Published on 12 August 2022.

Downloaded on 8/16/2022 1:55:52 PM

- J. Turner, G. Sverdrup, M. K. Mann, P. C. Maness, B. Kroposki, M. Ghirardi, R. J. Evans and D. Blake, *Int. J. Energy Res.*, 2008, 32, 379–407.
- 2 R. M. Navarro, M. Pena and J. Fierro, *Chem. Rev.*, 2007, **107**, 3952–3991.
- G. W. Huber, J. Shabaker and J. Dumesic, Science, 2003, 300, 2075–2077.
- A. Buttler and H. Spliethoff, *Renew. Sust. Energ. Rev.*, 2018, 82, 2440–2454.
- 5 B. You and Y. Sun, Acc. Chem. Res., 2018, **51**, 1571–1580.
- 6 C. C. McCrory, S. Jung, I. M. Ferrer, S. M. Chatman, J. C. Peters and T. F. Jaramillo, J. Am. Chem. Soc., 2015, 137, 4347–4357.
- 7 B. You, G. Han and Y. Sun, Chem. Commun., 2018, 54, 5943–5955.
- Q. Feng, X. Z. Yuan, G. Liu, B. Wei, Z. Zhang, H. Li and H. Wang, J. Power Sources, 2017, 366, 33–55.
- 9 J. R. Varcoe, P. Atanassov, D. R. Dekel, A. M. Herring, M. A. Hickner, P. A. Kohl, A. R. Kucernak, W. E. Mustain, K. Nijmeijer and K. Scott, *Energy Environ. Sci.*, 2014, **7**, 3135–3191.
- 10 E. W. Lees, B. A. Mowbray, F. G. Parlane and C. P. Berlinguette, *Nat. Rev. Mater.*, 2021, 1–10.
- 11 H. Liu and W. Li, Current Opinion in Electrochemistry, 2021, 30, 100795.
- 12 G.-F. Chen, Y. Luo, L.-X. Ding and H. Wang, ACS Catal., 2018, 8, 526–530.
- 13 W.-J. Liu, Z. Xu, D. Zhao, X.-Q. Pan, H.-C. Li, X. Hu, Z.-Y. Fan, W.-K. Wang, G.-H. Zhao and S. Jin, *Nat. Commun.*, 2020, **11**, 1–11.
- 14 B. You, X. Liu, X. Liu and Y. Sun, ACS Catal., 2017, 7, 4564–4570.
- 15 B. You, X. Liu, N. Jiang and Y. Sun, *J. Am. Chem. Soc.*, 2016, **138**, 13639–13646.
- 16 Y. Zhang, B. Zhou, Z. Wei, W. Zhou, D. Wang, J. Tian, T. Wang, S. Zhao, J. Liu and L. Tao, Adv. Mater., 2021, 2104791.
- 17 E. C. Ashby, F. Doctorovich, C. L. Liotta, H. M. Neumann, E. K. Barefield, A. Konda, K. Zhang, J. Hurley and D. D. Siemer, *J. Am. Chem. Soc.*, 1993, **115**, 1171–1173.
- 18 S. Kapoor, F. A. Barnabas, M. C. Sauer, D. Meisel and C. D. Jonah, J. Phys. Chem., 1995, 99, 6857–6863.
- 19 S. Zhang, Y. Ma, H. Zhang, X. Zhou, X. Chen and Y. Qu, Angew. Chem. Int. Ed., 2017, 56, 8245–8249.
- 20 X. Chen, H. Zhang, Z. Xia, S. Zhang and Y. Ma, Catal. Sci. Technol., 2019, 9, 783–788.
- 21 S. Liang, S. Chen, Z. Guo, Z. Lan, H. Kobayashi, X. Yan and R. Li, *Catal. Sci. Technol.*, 2019, **9**, 5292–5300.
- 22 L. E. Heim, N. E. Schlörer, J.-H. Choi and M. H. Prechtl, *Nat. Commun.*, 2014, **5**, 1–8.
- 23 M. Trincado, V. Sinha, R. E. Rodriguez-Lugo, B. Pribanic, B. de Bruin and H. Grützmacher, *Nat. Commun.*, 2017, **8**, 1–11.

- 24 L. Wang, M. Z. Ertem, R. Kanega, K. Murata, D. J. Szalda, J. T. Muckerman, E. Fujita and Y. Himeda, ACS, Gatal, 220, 322, 8, 8600–8605.
- 25 S. Kar, Q.-Q. Zhou, Y. Ben-David and D. Milstein, *J. Am. Chem. Soc.*, 2022, 144, **3**, 1288–1295.
- 26 A. S. May and E. J. Biddinger, ACS Catal., 2020, 10, 3212–3221.
- 27 K. Kondo, R. N. Akolkar, D. P. Barkey and M. Yokoi, *Copper electrodeposition for nanofabrication of electronics devices*, Springer, 2014.
- 28 S. Ghosh, Thin Solid Films, 2019, 669, 641-658.
- 29 H.-H. Hsu, K.-H. Lin, S.-J. Lin and J.-W. Yeh, J. Electrochem. Soc., 2001, 148, C47.
- S. Nakahara and Y. Okinaka, *Acta Metallurgica*, 1983, **31**, 713–724.
- 31 T. Wang, L. Tao, X. Zhu, C. Chen, W. Chen, S. Du, Y. Zhou, B. Zhou, D. Wang, C. Xie, P. Long, W. Li, Y. Wang, R. Chen, Y. Zou, X.-Z. Fu, Y. Li, X. Duan and S. Wang, *Nat. Catal.*, 2021, DOI: 10.1038/s41929-021-00721-y.
- S. Wang, T. Wang, L. Tao, J. Tian, K. Gu, X. Wei, P. Zhou, L. Gan,
   S. DU and Y. Zou, *Angew. Chem.*, 2021, 134, e202115636.
- 33 D.-H. Nam, B. J. Taitt and K.-S. Choi, ACS Catal., 2018, 8, 1197– 1206.
- 34 A. R. Poerwoprajitno, L. Gloag, J. Watt, S. Cychy, S. Cheong, P. V. Kumar, T. M. Benedetti, C. Deng, K. H. Wu and C. E. Marjo, Angew. Chem. Int. Ed., 2020, 59, 15487–15491.
- 35 H. G. Cha and K.-S. Choi, Nat. Chem., 2015, 7, 328–333.
- 36 H. Liu, T.-H. Lee, Y. Chen, E. W. Cochran and W. Li, *Green Chem.*, 2021, **23**, 5056–5063.
- 37 M. A. Bajada, S. Roy, J. Warnan, K. Abdiaziz, A. Wagner, M. M. Roessler and E. Reisner, *Angew. Chem.*, 2020, **132**, 15763–15771.
- 38 Y. Y. Birdja and M. T. Koper, *J. Am. Chem. Soc.*, 2017, **139**, 2030–2034.
- 39 J. P. Lange, E. Van Der Heide, J. van Buijtenen and R. Price, *ChemSusChem*, 2012, **5**, 150–166.
- 40 R. Mariscal, P. Maireles-Torres, M. Ojeda, I. Sádaba and M. L. Granados, *Energy Environ. Sci.*, 2016, **9**, 1144-1189.
- 41 Z. Zhang, E. W. Lees, F. Habibzadeh, D. A. Salvatore, S. Ren, G. L. Simpson, D. G. Wheeler, A. Liu and C. P. Berlinguette, *Energy Environ. Sci.*, 2022. DOI: 10.1039/D1EE02608A
- 42 Global Plastic Bottles Market-Growth, Analysis, Forecast to (2017–2022). 2016.
- 43 S. B. Scott, T. V. Hogg, A. T. Landers, T. Maagaard, E. Bertheussen, J. C. Lin, R. C. Davis, J. W. Beeman, D. Higgins and W. S. Drisdell, *ACS Energy Lett.*, 2019, **4**, 803-804.
- 44 S. H. Lee, J. C. Lin, M. Farmand, A. T. Landers, J. T. Feaster, J. E. Avilés Acosta, J. W. Beeman, Y. Ye, J. Yano and A. Mehta, J. Am. Chem. Soc., 2020, 143, 588-592.
- 45 J. H. Stenlid, E. C. dos Santos, R. M. Arán-Ais, A. Bagger, A. J. Johansson, B. R. Cuenya, J. Rossmeisl and L. G. M. Pettersson, *Electrochim. Acta*, 2020, **362**, 137111.
- 46 A. M. Román, J. C. Hasse, J. W. Medlin and A. Holewinski, ACS Catal., 2019, 9, 10305–10316.
- 47 M. Neurock, M. Janik and A. Wieckowski, *Faraday Discuss.*, 2009, **140**, 363–378.
- 48 A. M. Román, N. Agrawal, J. C. Hasse, M. J. Janik, J. W. Medlin and A. Holewinski, *J. Catal.*, 2020, **391**, 327–335.
- 49 A. J. Bard and L. R. Faulkner, *Electrochemical methods*, 2001, **2**, 580–632.
- 50 J. Ryu, D. T. Bregante, W. C. Howland, R. P. Bisbey, C. J. Kaminsky and Y. Surendranath, *Nat. Catal.*, 2021, **4**, 742–752.
- 51 L. Zhang, K. Lee and J. Zhang, *Electrochim. Acta*, 2007, **52**, 7964–7971.
- 52 H. Chen, J. Wang, Y. Yao, Z. Zhang, Z. Yang, J. Li, K. Chen, X. Lu, P. Ouyang and J. Fu, ChemElectroChem, 2019, 6, 5797–5801.
- 53 B. Zhou, Y. Zhang, T. Wang, W. Zhou, J. Liu, Y. Zou, L. Tao, Y. Lu and S. Wang, *Chem Catal.*, 2021. https://doi.org/10.1016/j.checat.2021.11.003

Open Access Article. Published on 12 August 2022. Downloaded on 8/16/2022 1:55:52 PM

Journal Name ARTICLE

- 54 F. Dattila, R. García-Muelas and N. r. López, ACS Energy Lett., 2020. 5. 3176–3184.
- 55 D. Cheng, Z.-J. Zhao, G. Zhang, P. Yang, L. Li, H. Gao, S. Liu, X. Chang, S. Chen and T. Wang, *Nat. Commun.*, 2021, **12**, 1–8.
- 56 H. Liu, J. Park, Y. Chen, Y. Qiu, Y. Cheng, K. Srivastava, S. Gu, B. H. Shanks, L. T. Roling and W. Li, ACS Catal., 2021, 11, 8431–8442.
- 57 J. Lee, H. Liu, Y. Chen and W. Li, ACS Appl. Mater. Interfaces., 2022, 14, 14210–14217
- 58 S. Lamaison, D. Wakerley, J. Blanchard, D. Montero, G. Rousse, D. Mercier, P. Marcus, D. Taverna, D. Giaume and V. Mougel, *Joule*, 2020, 4, 395–406.
- 59 Z. Weng, X. Zhang, Y. Wu, S. Huo, J. Jiang, W. Liu, G. He, Y. Liang and H. Wang, *Angew. Chem.*, 2017, **129**, 13315–13319.
- 60 A. Herzog, A. Bergmann, H. S. Jeon, J. Timoshenko, S. Kühl, C. Rettenmaier, M. Lopez Luna, F. T. Haase and B. Roldan Cuenya, Angew. Chem., Int. Ed., 2021, 60, 7426–7435.
- 61 S. Brittman, A. J. Smith, S. Milenkovic and A. W. Hassel, *Electrochim. Acta*, 2007, **53**, 324–329.
- 62 L. Wang, H. Peng, S. Lamaison, Z. Qi, D. M. Koshy, M. B. Stevens, D. Wakerley, J. A. Z. Zeledón, L. A. King and L. Zhou, *Chem Catal.*, 2021, 1, 663-680.
- 63 J. Woo, B. C. Moon, U. Lee, H.-S. Oh, K. H. Chae, Y. Jun, B. K. Min and D. K. Lee, ACS Catal., 2022, 12, 4078-4091.
- 64 G. Antczak and G. Ehrlich, Surface diffusion: metals, metal atoms, and clusters, Cambridge University Press, 2010.
- 65 C. G. Morales-Guio, E. R. Cave, S. A. Nitopi, J. T. Feaster, L. Wang, K. P. Kuhl, A. Jackson, N. C. Johnson, D. N. Abram and T. Hatsukade, *Nat. Catal.*, 2018, 1, 764-771.
- 66 G. Liu, F. Zheng, J. Li, G. Zeng, Y. Ye, D. M. Larson, J. Yano, E. J. Crumlin, J. W. Ager and L.-w. Wang, *Nat. Energy*, 2021, 1–9.
- 67 Y. Lin, C. Deng, L. Wu, Y. Zhang, C. Chen, W. Ma and J. Zhao, Energy Environ. Sci., 2020, 13, 2602–2617.
- 68 M. B. Smith, March's advanced organic chemistry: reactions, mechanisms, and structure, John Wiley & Sons, 2020.
- 69 H. Liu, T. H. Lee, Y. Chen, E. W. Cochran and W. Li, ChemElectroChem, 2021, 8, 2817–2824.

- 70 Porous metal electrodes enable efficient electrolysis or carbon capture solutions, EES, 2022, Cuptiss<sub>10.1039</sub>/D2EE01427K
- 71 Z. Y. Yu, Y. Duan, X. Y. Feng, X. Yu, M. R. Gao and S. H. Yu, Adv. Mater., 2021, 2007100.
- 72 T. Janoschka, N. Martin, U. Martin, C. Friebe, S. Morgenstern, H. Hiller, M. D. Hager and U. S. Schubert, *Nature*, 2015, **527**, 78-81.
- 73 Q. Duan, S. Ge and C.-Y. Wang, J. Power Sources, 2013, 243, 773–778.
- 74 D. A. Salvatore, C. M. Gabardo, A. Reyes, C. P. O'Brien, S. Holdcroft, P. Pintauro, B. Bahar, M. Hickner, C. Bae and D. Sinton, *Nat. Energy*, 2021, **6**, 339–348.
- 75 E. C. Tan, M. Talmadge, A. Dutta, J. Hensley, J. Schaidle, M. Biddy, D. Humbird, L. J. Snowden-Swan, J. Ross and D. Sexton, Process Design and Economics for the Conversion of Lignocellulosic Biomass to Hydrocarbons via Indirect Liquefaction. Thermochemical Research Pathway to High-Octane Gasoline Blendstock Through Methanol/Dimethyl Ether Intermediates, National Renewable Energy Lab.(NREL), Golden, CO (United States), 2015.
- 76 B. James, W. Colella, J. Moton, G. Saur and T. Ramsden, *PEM electrolysis H₂A production case study documentation*, National Renewable Energy Lab.(NREL), Golden, CO (United States), 2013.
- 77 G. Saur and C. Ainscough, *US Geographic analysis of the cost of hydrogen from electrolysis*, National Renewable Energy Lab.(NREL), Golden, CO (United States), 2011.
- 78 Paper W. INNOVATIONS Hydrogen Production Cost by AEM Water Electrolysis [Internet]. 2020. Available from: www.ionomr.com
- 79 Organic Chemical 2-Furoic acid CAS NO.88-14-2, alibaba.com, accessed 2 October 2021 [Internet]. Available from: https://www.alibaba.com/product-detail/Organic-Chemical-2-Furoic-acid-
  - CAS\_60496406282.html?spm=a2700.galleryofferlist.normal\_offer.d\_title.3ac32bc3qlOShr